

# 1           **Characterization and Correction of OMPS**

## 2           **Nadir Mapper Measurements for Ozone Profile**

### 3                                   **Retrievals**

4  
5   Juseon Bak<sup>a,#</sup> ([juseon.bak@cfa.harvard.edu](mailto:juseon.bak@cfa.harvard.edu)), Xiong Liu<sup>b</sup> ([xliu@cfa.harvard.edu](mailto:xliu@cfa.harvard.edu)),

6   Jae-Hwan Kim<sup>a,\*</sup> ([jaekim@pusan.ac.kr](mailto:jaekim@pusan.ac.kr)), David P. Haffner<sup>c</sup> ([david.haffner@ssaihq.com](mailto:david.haffner@ssaihq.com)),

7   Kelly Chance<sup>b</sup> ([kchance@cfa.harvard.edu](mailto:kchance@cfa.harvard.edu)), Kai Yang<sup>d</sup> ([KaiYang@umd.edu](mailto:KaiYang@umd.edu)),

8   Kang Sun<sup>b</sup> ([Kang.sun@cfa.harvard.edu](mailto:Kang.sun@cfa.harvard.edu))

9   <sup>a</sup>*Pusan National University, Busan, Korea*

10   <sup>b</sup>*Harvard-Smithsonian Center for Astrophysics, Cambridge, MA, United States*

11   <sup>c</sup>*Science Systems and Applications, Inc., 10210 Greenbelt Rd, Lanham, MD 20706, United States*

12   <sup>d</sup>*Department of Atmospheric and Oceanic Science, University of Maryland College Park, College Park,*  
13   *Maryland, USA*

14   #Currently at Harvard-Smithsonian Center for Astrophysics, Cambridge, MA, United States

15   \*Corresponding Author

16                                   Abstract

17   This paper verifies and corrects the Ozone Mapping and Profiler Suite (OMPS) Nadir Mapper (NM)  
18   Level 1B v2.0 measurements with the aim of producing accurate ozone profile retrievals using an  
19   optimal estimation based inversion method to fit measurements in the spectral range 302.5-340 nm. The  
20   evaluation of available slit functions demonstrates that preflight-measured slit functions well represent  
21   OMPS measurements compared to derived Gaussian slit functions. Our initial OMPS fitting residuals  
22   contain significant wavelength and cross-track dependent biases, resulting in serious cross-track striping  
23   errors in the tropospheric ozone retrievals. To eliminate the systematic component of the fitting residuals,  
24   we apply “soft calibration” to OMPS radiances. With the soft calibration the amplitude of fitting  
25   residuals decreases from ~1 % to 0.2 % over low/mid latitudes, and thereby the consistency of  
26   tropospheric ozone retrievals between OMPS and the Ozone Monitoring Instrument (OMI) is  
27   substantially improved. A common mode correction is also implemented for additional radiometric  
28   calibration; it improves retrievals especially at high latitudes where the amplitude of fitting residuals  
29   decreases by a factor of ~2. We estimate the noise floor error of OMPS measurements from standard

30 deviations of the fitting residuals. The derived error in the Huggins band (~0.1 %) is twice the OMPS  
31 L1B measurement error. OMPS noise floor errors better constrains our retrievals, leading to improving  
32 information content of ozone and reducing fitting residuals. The final precision of the fitting residuals  
33 is less than 0.1 % in the low/mid latitude, with ~1 degrees of freedom for signal for the tropospheric  
34 ozone, meeting the general requirements for successful tropospheric ozone retrievals.

## 35 **1. Introduction**

36 Atmospheric ozone has very different roles depending upon its altitude. About 90 % of the total  
37 ozone is in the stratosphere, protecting the Earth's life from harmful solar ultraviolet (UV) radiation  
38 that can cause skin cancer and immune system suppression. The remaining 10 % in the troposphere  
39 shows dangerous effects as a major component of photochemical smog at surface level and as a short-  
40 lived greenhouse gas in the upper troposphere, whereas in the middle troposphere it plays a beneficial  
41 role in chemically cleaning the atmosphere as a precursor of hydroxyl radicals (OH). Therefore, vertical  
42 ozone profiles should be monitored to improve our understandings of the chemical and physical  
43 functions of this important trace gas. Space-based monitoring of ozone profiles including the  
44 troposphere from backscattered UV radiation has been available since the launch of Global Ozone  
45 Monitoring Experiment (GOME) (European Space Agency, 1995) on board the Second European  
46 Remote Sensing Satellite (ERS-2) in April 1995. Its successors continued the role of GOME for  
47 atmospheric ozone monitoring with Scanning Imaging Absorption SpectroMeter for Atmospheric  
48 CHartographyY (SCIAMACHY) (Bovensmann et al., 1999) aboard the Environmental Satellite  
49 (ENVISAT), GOME-2s (EUMETSAT, 2006) aboard the MetOp-A and MetOp-B, and Ozone  
50 Monitoring Instrument (OMI) (Levelt et al, 2006) flown on the EOS Aura spacecraft. The good  
51 performance of OMI ozone profile retrievals in both stratosphere and troposphere has been  
52 demonstrated through extensive validation efforts using ozonesondes, aircraft, satellite data, and  
53 ground-based total ozone data (Pittman et al., 2009; Liu et al., 2010b; Bak et al., 2013b; 2015; Huang  
54 et al., 2017a, b). However, a portion of OMI radiance measurements has been affected by the partial  
55 blockage of the instrument's entrance slit, a problem termed the row anomaly, which started in 2007  
56 and grew serious in January 2009 (Schenkeveld, 2017). The Ozone Mapping and Profiler Suite (OMPS)  
57 aboard the Suomi National Polar-Orbiting Partnership (NPP) satellite launched in 2011 (Flynn, et al.,  
58 2014) represents the next generation of US instruments to continue the role of OMI in monitoring total  
59 ozone and ozone vertical profiles, together with the TROPOspheric Monitoring Instrument (TROPOMI)  
60 to be launched on board the Sentinel-5 Precursor satellite in 2017 (Veefkind et al., 2012). OMPS is a

61 sensor suite which consists of three instruments, the Nadir Mapper (OMPS-NM), the Nadir Profiler  
62 (OMPS-NP), and the Limb Profiler (OMPS-LP). The OMPS-NM is designed to measure the daily  
63 global distribution of total column ozone with an  $110^\circ$  cross-track field of view (FOV), similar to OMI  
64 and the Total Ozone Monitoring Spectrometer (TOMS) series (Bhartia and Wellemeyer, 2002). OMPS-  
65 NP is an ozone profiler sensor, measuring the vertical ozone profiles in the upper stratosphere, similar  
66 to the Solar Backscatter Ultraviolet (SBUV/2) series (Bhartia et al., 2013). The OMPS-LP is designed  
67 to measure ozone profiles in the stratosphere and upper troposphere at high vertical resolution, similar  
68 to the Microwave Limb Sounder (MLS). Both OMPS-NP and OMPS-LP are ozone profile sensors, but  
69 lack sensitivity to the troposphere due to the spectral coverage of 250-290 nm and the viewing geometry,  
70 respectively. Therefore, OMPS-NM is the only candidate for global monitoring of ozone profiles down  
71 to the troposphere even though its spectral resolution of 1.0 nm does not fully resolve the ozone  
72 absorption band features in the Huggins band and its spectral coverage of 300-380 nm is insufficient to  
73 retrieve stratospheric ozone profiles. The retrieving of ozone profiles including tropospheric ozone from  
74 OMPS-NM measurements has not yet been presented in the literature. The present effort fills the gap  
75 between OMI and upcoming satellite observations.

76 The final goal of this study is to demonstrate the successful performance of ozone profiles and  
77 tropospheric ozone retrievals from only OMPS-NM measurements. Thus, we refer to OMPS-NM  
78 simply as OMPS hereafter. The retrieval algorithm used in this study is based on the Smithsonian  
79 Astrophysical Observatory (SAO) ozone profile algorithm that was developed for GOME (Liu et al.,  
80 2005) and OMI (Liu et al., 2010a). The SAO OMI algorithm is based on an optimal estimation inversion  
81 (Rodgers, 2000) combined with accurate wavelength/radiometric calibration, forward model simulation,  
82 and good a priori knowledge. This algorithm has been implemented for ozone profile and SO<sub>2</sub> retrievals  
83 from GOME-2 instrument (Cai et al., 2011; Nowlan et al., 2011) and will be adapted to ozone profile  
84 retrievals from upcoming geostationary UV/VIS spectrometers including the Geostationary  
85 Environmental Monitoring Spectrometer (GEMS) (Bak et al 2013a) and Tropospheric Emissions:  
86 Monitoring of POLLution (TEMPO) instrument (Chance et al., 2013, Zoogman et al., 2017) for  
87 monitoring air quality over North America and East Asia, respectively. OMPS has a similar instrument  
88 concept to OMI, GEMS, and TEMPO and hence the application of the similar retrieval algorithms to  
89 these measurements will provide an excellent opportunity for long-term trend analysis of ozone profiles,  
90 especially in the troposphere. The OMI algorithm is very similar to our OMPS algorithm, but it needs  
91 additional optimization for OMPS. In this paper we focus largely on characterizing OMPS  
92 measurements (1) through the cross-correlation between OMPS irradiances and a high-resolution solar  
93 reference to be used in the verification of OMPS slit function measurements and the characterization of

94 the wavelength registration and (2) through extracting the systematic and random components of fitting  
95 residuals between measured and calculated normalized radiances to be used in radiometric and  
96 measurement error calibrations, respectively. Several companion papers to follow will deal with the  
97 detailed error analysis, retrieval characteristics of the retrieved ozone profiles, and validation of  
98 retrievals.

99 The paper is divided into four sections: First, we give a description of OMPS-NM Level 1B (L1B)  
100 v2.0 data (Jaross, 2017) and the ozone profile algorithm in Sect. 2. Section 3 discusses the  
101 wavelength/slit function calibrations and measurement corrections for radiance and measurement error,  
102 respectively. Conclusions are in Sect. 4.

103

## 104 **2. Data and Method**

### 105 **2.1 OMPS measurements**

106 The Suomi NPP satellite is a NOAA/NASA scientific partnership, launched in 2011 into a 824 km sun-  
107 synchronous polar orbit with ascending node equator-crossing time at 13:30 local time. Routine  
108 operations began in 2012. Suomi NPP carries five instruments: The Visible/Infrared Imager Radiometer  
109 Suite (VIIRS), the Cross-track Infrared Sounder (CrIS), the Advanced Technology Microwave Sounder  
110 (ATMS), the Ozone Mapping and Profile Suite (OMPS), and the Clouds and the Earth Radiant Energy  
111 System (CERES). OMPS is a key instrument on Suomi NPP. The sensor suite has both nadir and limb  
112 modules. The nadir module combines two sensors: The Nadir Mapper for measuring total column ozone,  
113 and the Nadir Profiler for ozone vertical profile. The Limb Profiler module is designed to measure  
114 vertical ozone profiles with high vertical resolution from the upper troposphere/lower stratosphere to  
115 the mesosphere. The OMPS-NM employs a 2-D CCD that samples spectrally in one dimension and  
116 spatially in the other, similar to OMI. It has a  $110^\circ$  cross-track field of view, resulting in 2800 km  
117 instantaneous swath coverage at the earth's surface; this is sufficient to provide daily global coverage.  
118 It makes 400 swath lines per orbit with 36 cross-track measurements per swath line, resulting in a nadir  
119 footprint of  $50 \text{ km} \times 50 \text{ km}$  in its nominal configuration. Note that OMPS L1B data used in this  
120 investigation contain 36 cross-track pixels, because the L1B processing in the NASA Ozone SIPS  
121 retains the two central (near-nadir) instantaneous fields of views (IFOVs,  $30 \text{ km} \times 50 \text{ km}$  and  $20 \text{ km} \times$   
122  $50 \text{ km}$ ), without aggregating them into the nominal  $50 \text{ km} \times 50 \text{ km}$  pixel. The spectral coverage is from  
123 300 to 380 nm with a spectral resolution of  $\sim 1.0 \text{ nm}$  and a sampling of 0.42 nm. The OMPS level 0 to  
124 1b processor was recently updated from version 1.0 to 2.0. The satellite measurements from the OMPS-

125 NM instrument used in this study are from version 2 of the NMEV-L1B data product (Jaross, 2017)  
126 available from the NASA Goddard Earth Sciences Data and Information Services Center (GES  
127 DISC). The data consist of calibrated Earth-view radiance and solar irradiance data measured by the  
128 instrument between 300-380 nm. Seftor et al. (2014) documented many aspects of the previous version  
129 of the dataset that remain the same, but a number of changes for the V2 dataset do reflect advances in  
130 the characterization of the NM sensor (Seftor and Jaross, 2017) which are relevant to this study. These  
131 are summarized as follows: 1) recalculation of instrument band-pass functions in the 300-310 nm region  
132 affected by the dichroic element of the nadir instrument, 2) improved wavelength registration, 3) an  
133 update to the instrument radiance calibration, and 4) improvement to the stray light correction. The  
134 wavelengths below 302 nm are not used in this study, according to the recommendation of the OMPS  
135 science team.

## 136 **2.2 OMPS simulations**

137 We use the Vector LInearized Discrete Ordinate Radiative Transfer (VLIDORT) model (Spurr, 2006;  
138 2008) to simulate OMPS radiances. VLIDORT is also able to simulate the analytic derivatives of  
139 radiance with respect to any atmospheric or surface parameter due to its full linearization capability.  
140 The polarization of light is taken into account in VLIDORT calculation, but the Ring spectrum is  
141 modeled using a single scattering RRS model (Sioris and Evans, 2000). We consider only Rayleigh  
142 scattering (no aerosol) and ozone absorption (no other trace gases), with Lambertian reflectance  
143 assumed for the surface and for clouds. Clouds are treated as a Lambertian reflector at cloud top, with  
144 a fixed albedo of 0.8 unless it is fully cloudy so that the cloud albedo ( $>0.80$ ) can be derived. Cloud  
145 fraction is required to simulate partial clouds as the weighted average between clear and cloudy scenes  
146 using the Independent Pixel Approximation (IPA). The forward model inputs used in VLIDORT are  
147 listed in Table 1.

## 148 **2.3 OMPS ozone profile retrievals**

149 The inversion from Backscattered UV measurements to the state of the atmosphere is performed  
150 using the well-known optimal estimation method (Rodgers, 2000). It calculates the a posteriori solution  
151 by iteratively and simultaneously minimizing the cost function consisting of the sum of the squared  
152 differences between measured and simulated radiances and between retrieved and a priori state vectors,

153 constrained by measurement error covariance matrix and a priori error covariance matrix. The a  
 154 posteriori solution and cost function can be written:

$$155 \quad X_{i+1} = X_i + (K_i^T S_y^{-1} K_i + S_a^{-1})^{-1} [K_i^T S_y^{-1} (Y - R(X_i)) - S_a^{-1} (X_i - X_a)] \quad (1)$$

$$156 \quad \chi^2 = \left\| S_y^{-\frac{1}{2}} \{K_i(X_{i+1} - X_i) - [Y - R(X_i)]\} \right\|_2^2 + \left\| S_a^{-\frac{1}{2}} (X_{i+1} - X_a) \right\|_2^2. \quad (2)$$

157 The inputs to the optimal estimation are defined as follows.  $\mathbf{X}$  is the state vector to be retrieved,  
 158 consisting of ozone profiles as well as other geophysical parameters and spectroscopic parameters  
 159 affecting the observed radiances and hence the retrieval of ozone profile. The 24 partial columns of  
 160 ozone in DU are retrieved at 25 pressure levels that are initially set to be  $P_i = 2^{-i/2}$  atm for  $i =$   
 161  $0, 1, \dots, 23$  (1 atm = 1013.25 hPa) with the top of the atmosphere at 0.087 hPa for  $P_{24}$ . The geophysical  
 162 parameters include effective surface albedo and cloud fraction. The calibration parameters consists of  
 163 two wavelength shift parameters between radiances and irradiances and between radiances and ozone  
 164 cross sections and two scaling parameters for the Ring effect that account for filling-in of Fraunhofer  
 165 lines in the solar spectrum due to rotational Raman scattering and mean fitting residuals that may not  
 166 be accounted for properly in radiometric calibration. The a priori data for ozone is one of the key optimal  
 167 estimation inputs because the retrieval solution comes mainly from a priori information rather than  
 168 measurement information where the instrument sensitivity to the true ozone profile is insufficient. The  
 169 a priori value ( $X_a$ ) and a priori error covariance ( $S_a$ ) of ozone is taken from the tropopause-based ozone  
 170 profile climatology that is optimized to represent the dynamical ozone variability in the upper  
 171 troposphere and lower stratosphere (Bak et al., 2013b). The measurement vector  $Y$  is defined as the  
 172 logarithm of the earthshine radiances normalized to the daily solar irradiance.  $S_y$  is a measurement  
 173 error covariance matrix that is assumed to be a diagonal matrix with diagonal elements being the squares  
 174 of the assumed measurement errors. We use OMI noise floor errors (0.4 % below 310 nm, 0.2 % above,  
 175 Huang et al., 2017a) as our preliminary measurement constraint and then derive OMPS noise floor  
 176 errors specified in Section 3.4.  $R(X)$  is the calculated radiances corresponding to  $X$ .  $K$  is a weighting  
 177 function matrix representing partial derivatives of the forward model with respect to the atmospheric  
 178 parameters,  $K_{ij} = \partial R_i(X) / \partial X_j$ . More detailed descriptions can be detailed in Liu et al. (2010a).

179

## 180 **3. Results**

### 181 **3.1 Slit Function and Wavelength Calibration`**

182 It is essential to investigate the best knowledge of the instrument slit function to convolve a high-  
183 resolution solar reference spectrum for wavelength calibration as well as to convolve high-resolution  
184 trace gas cross sections for simulation of earthshine spectra. A triangular bandpass with a fixed  
185 bandwidth of 1.1 nm has been typically used for Total Ozone Monitoring Instrument (TOMS), SBUV,  
186 and SBUV/2 monochromators. Slit functions of spectrometers such as OMI and GOME1/2 have been  
187 measured prior to launch using a tunable laser or analytically derived assuming a Gaussian-type shape  
188 if measured slit functions are unavailable or inaccurate. The OMPS preflight slit functions were  
189 characterized for each CCD pixels (196 band centers and 36 cross-track positions), which has been  
190 adopted and modified for OMPS trace-gas retrievals such as in Yang et al. (2013; 2014) and Gonzalez  
191 Abad et al. (2016). The slit function modification is accomplished in the previous works (Yang et al.,  
192 2013, 2014) by stretching and shrinking the slit widths, i.e., by applying a wavelength-dependent  
193 scaling factor to the OMPS measured slit functions. According to Yang et al. (2013; 2014), we fit the  
194 scaling factor as a slit parameter so that variations in measured slit functions before and after launch  
195 could be taken into account.

196 Figure 1a shows an example of measured OMPS slit functions at 320 nm, illustrating that their  
197 shapes seem to be Gaussian and vary considerably over cross-track pixels, especially near the wings.  
198 Note that the 36 cross-track positions are denoted from 1 at the left edge and 36 at the right edge. The  
199 slit function shapes at 17<sup>th</sup> cross-track position are nearly consistent over wavelengths that we are  
200 focusing on for ozone retrievals (Fig. 1.b). Figure 1c displays the full width at half maximum (FWHM)  
201 including dependencies in both dimensions of the detector arrays. The spectral variation of the slit  
202 widths is insignificant (FWHMs vary by less than 0.01 nm), whereas average slit widths vary  
203 significantly across track by over 0.1 nm. This characteristic of measurement slit functions confirms  
204 that we should consider their cross-track dependence for OMPS slit functions, but their wavelength  
205 dependence is ignorable so that we can avoid the time-consuming convolution process.

206 We evaluate the usefulness of these measured slit functions for fitting both OMPS radiance and  
207 irradiance against the analytical slit functions assusing both standard Gaussian and super Gaussian  
208 distributions. We note all the Gaussian shapes used in this analysis are assumed to be symmetric. The  
209 Gaussian slit function is expressed as

210 
$$S(\lambda) = \frac{k}{2w\Gamma\left(\frac{1}{k}\right)} \exp\left[-\left|\frac{\Delta\lambda}{w}\right|^k\right], \quad (3)$$

211 where  $k$  is the shape factor and  $w$  is the slit width, with relative wavelength to band center wavelength,  
 212  $\Delta\lambda$ . This function can describe a wide variety of shapes just by varying  $k$ ; for  $k=2$  it becomes the  
 213 standard Gaussian and  $w$  represents the half width at 1/e intensity (FWHM =  $2\sqrt{\ln 2} w$ ). Compared  
 214 to the standard Gaussian, the super Gaussian has broader peaks at the top and thinner wings if  $k$  is larger  
 215 than 2 whereas it has sharper peaks and longer tails if  $k$  is smaller than 2.  $w$  of the super Gaussian  
 216 function represents the half-width at 1/e<sup>th</sup> intensity (FWHM =  $2^k\sqrt{\ln 2}$ ). The symmetric or asymmetric  
 217 standard Gaussian has been commonly assumed to derive OMI, GOME, and GOME-2 slit functions  
 218 (Liu et al., 2005;2010; Nowlan et al., 2011; Cai et al., 2012; Munro et al., 2016). Recently the hybrid  
 219 combination of standard and flat-top Gaussian functions has been implemented for characterizing OMI  
 220 laboratory measurements of slit functions (Dirksen et al., 2006) and deriving airborne instrument slit  
 221 functions (Liu et al., 2015a;2015b; Nowlan et al., 2016). The concept of this hybrid Gaussian function  
 222 is very similar to the super Gaussian, but is a rather complex with more slit parameters. The super  
 223 Gaussian function was introduced and tested as an analytical slit function by Beirle et al. (2017) and  
 224 Sun et al. (2017a;b).

225 In general, when accurate measurements of slit functions are not available, the instrument line shape  
 226 of satellite observation is typically assumed to be the same for both radiance and irradiance  
 227 measurements, and then can be better determined from irradiances due to lack of atmospheric  
 228 interference.. We simultaneously and iteratively determine the wavelength and slit calibration  
 229 parameters through cross-correlation of the measured OMPS irradiances to simulated solar irradiances  
 230 from a well calibrated, high-resolution solar irradiance reference spectrum (Chance and Kurucz, 2010).  
 231 The simulation of solar irradiance,  $I_s$  is described as

232 
$$I_s(\lambda) = AI_o(\lambda + \Delta\lambda) \times \sum_{i=0}^2 P_i(\lambda - \lambda_{avg})^i, \quad (4)$$

233 where  $I_o$  is the convolved high-resolution solar reference spectrum with assumed slit functions,  $A$  is  
 234 the scaling parameter for  $I_o$ .  $\lambda + \Delta\lambda$  Indicates the process of wavelength calibration (e.g. shift and  
 235 squeeze); only the wavelength shift is considered in this study.  $P_i$  represents the coefficients of a scaling  
 236 polynomial (third order in this study). This approach was firstly introduced by Caspar and Chance  
 237 (1997), and is widely used for wavelength and slit function calibrations in trace gas retrievals from  
 238 UV/visible measurements.



239 In this experiment, the slit parameters,  $w$  and  $k$  or slit scaling are fitted from daily measured  
240 OMPS irradiances over the wavelength range 302-340 nm at each cross-track position. Note that this  
241 slit calibration ignores the wavelength dependence for deriving analytic slit functions and slit scaling to  
242 the measured slit functions; this is a good approximation based on Fig. 1b as the wavelength dependence  
243 of the slit functions is small. But the variation of the slit shape with wavelength could be considered  
244 with OMPS preflight measured slit functions given for every CCD dimension if it becomes necessary.  
245 The left panels of Fig. 2 compare the derived slit parameters from OMPS irradiances using different  
246 functions. The red line of Fig. 2.a.1 shows that a slight change of the preflight-measured slit functions  
247 is required to model the OMPS irradiance measurements, by up to 4% at both edges. Therefore the  
248 benefit of fitting measured slit functions over fixing them is found to be trivial ( $\sim 0.001$  %) at nadir  
249 cross-track pixels (12-30<sup>th</sup>); for edge pixels, the improvement in fitting residuals is more noticeable, up  
250 to 0.18%. The shape factor ( $k$ ) of the derived super Gaussian functions is found to be  $\sim 2.3$  for left swath  
251 and  $\sim 2.5$  for right swath (Fig. 2.b.1), implying that they have broader peaks and thinner wings compared  
252 to the standard Gaussian if slit widths are equal. The slit widths of three different slit functions show  
253 similar variations with respect to cross-track positions. The FWHMs vary from widest at  $\sim 12^{\text{th}}$  cross-  
254 track position to narrowest at the edges, but they are significantly narrower at the rightmost cross-track  
255 positions than at the leftmost ones. Compared to the standard Gaussian slit widths, the super Gaussian  
256 slit widths show a much better agreement with measured slit widths; the average difference of slit widths  
257 between measured and super (standard) Gaussian functions is  $\sim 0.01$  (0.05) nm. In Fig. 3, an example  
258 of the derived slit functions and fitted preflight slit functions shows that the shapes are very similar.

259 The wavelength calibrations using different slit functions are characterized for the ozone fitting  
260 window and are shown in Fig. 4b. The shift parameter is determined from irradiance and radiance at  
261 second cross-correlation step after slit parameters are determined from irradiances at first cross-  
262 correlation step. Note that the wavelength shifts fitted between first and second steps are very similar,  
263 indicating little correlation between slit and wavelength calibration parameters. This analysis indicates  
264 that the accuracy of wavelength registration in ozone fitting wavelengths is 0.03-0.06 nm for earthshine  
265 measurements and  $< 0.02$  nm for solar measurements with consistent variation over all cross-track  
266 pixels. These wavelength errors are larger than those reported by Seftor et al. (2014), due to different  
267 fitting windows. They use 350-380 nm where prominent solar Fraunhofer absorption lines exist and the  
268 interference with ozone absorption lines are negligible. Furthermore, the wavelength calibration results  
269 using OMPS measured slit functions show different characteristics from those using both Gaussian-  
270 type slit functions, especially over left cross-track pixels. The different wavelength shifts are likely  
271 because the original OMPS slit functions show slight asymmetry and are used in the wavelength

272 calibration of L1B data. There exists a  $\sim 0.07$  nm shift between irradiances and radiance. In ozone  
273 retrieval algorithm we shift neither radiance nor irradiance to a reference spectra before retrievals, but  
274 the shift between irradiance and radiance is adjusted during ozone retrievals to account for the on-orbit  
275 variations of wavelength shifts as mentioned in Sect. 2.3.

276 The right columns of Fig. 2 compare the impact of different slit functions on spectral fitting residuals  
277 of solar irradiances, together with the average fitting residuals as a function of cross-track position in  
278 Fig.4.a. Measured solar spectra are mostly within an average of  $\sim 1\%$  of modeled solar spectra, except  
279 for the first few wavelengths. Based on these fitting results, we revise the fitting window to 302.5-340  
280 nm. The fitting residuals using a derived standard Gaussian function are the worst for all cross-track  
281 positions. On the other hand, the super Gaussian slit function similarly represents the measured slit  
282 function, but slightly improves the fitting accuracy at the 6~18 cross-track positions (Fig. 4.a). However,  
283 the benefit of using the super Gaussian function for fitting OMPS radiances over the standard Gaussian  
284 function is insignificant within 0.02 % (not shown here). These results agree well with Beirle et al.  
285 (2017), who demonstrated the similar benefit of using Standard and Super Gaussian slit functions on  
286 OMI and GOME-2 measurements. Moreover, the impact of using different slit functions could be less  
287 important for OMPS than OMI and GOME-2 due to its coarser spectral resolution.

288 In summary, super Gaussian functions are recommended for the OMPS instrument slit functions  
289 than the standard Gaussian functions if the on-orbit instrument slit functions largely deviate from the  
290 preflight-measured slit functions due to instrument degradation or thermal-induced variation. In the rest  
291 of this paper, the measured slit function is used for the analysis of OMPS measurements.

292

### 293 **3.2 Soft Calibration**

294 The OMPS instrument 2-D CCD detector array could be susceptible to artificial cross-track  
295 dependent errors that are commonly seen in OMI trace gas retrievals. To eliminate this impact on the  
296 OMI L2 product, soft calibration and post-processing cross-track smoothing have been typically  
297 implemented: the first correction removes the systematic wavelength and cross-track dependent  
298 component in measured radiances (Liu et al., 2010; Cai et al., 2012), whereas the second correction  
299 removes cross-track dependent biases in retrievals (Kurosu et al., 2004; Hormann et al., 2016). Figure  
300 5 compares our preliminary tropospheric and stratospheric ozone column retrievals with OMI retrievals  
301 on 14 March 2013. OMPS stratospheric retrievals show an excellent consistency with OMI even though  
302 OMPS measurements does not cover much of the Hartley ozone absorption wavelengths where most of

303 the vertical information of stratospheric ozone comes from. This is because the separation of  
304 stratospheric ozone columns from tropospheric ozone columns is still mainly determined from  
305 wavelengths longer than 300 nm (Bak et al., 2013a). On the other hand, tropospheric ozone retrievals  
306 are positively biased with respect to OMI, by amounts largely dependent on the OMI cross-track  
307 position. Therefore, we decide to include a soft-calibration correction in our retrievals to eliminate  
308 wavelength and cross-track dependent errors in OMPS radiances. A general approach to the soft  
309 calibration is to characterize systematic differences between measured and computed radiances for  
310 scenes where we could assume that all parameters are known; the tropics were typically selected since  
311 ozone variability is relatively small (Liu et al., 2010). OMPS normalized radiances are simulated with  
312 collocated OMI ozone profiles averaged and interpolated onto  $5^\circ \times 5^\circ$  grid cells to fill in bad pixels  
313 mostly caused by the row anomaly. Other forward model inputs are described in Sect. 2. We use 25 days  
314 of data between 1 March 2013 and 25 March 2013 under the following conditions: latitude  $<15^\circ\text{N/S}$ ,  
315 solar zenith angle (SZA)  $<40^\circ$ , cloud fraction  $<0.1$ , and surface reflectivity  $<0.1$ . The systematic and  
316 random components of measured-to-simulated radiance ratios are displayed in Fig. 6. Agreement is  
317 mostly at the  $\pm 2\%$  level below 310 nm, except at wavelengths shorter than  $\sim 302.5$  nm where the  
318 systematic biases increase sharply due to the overcorrection of straylight in OMPS v2.0 data processing.  
319 For wavelengths longer than 310 nm, OMPS observations show negative biases with maximum of  $\sim 3\%$   
320 at 315 nm. The standard deviations of mean differences steadily increase from longer wavelengths to  
321 302.5 nm (2-2.5%) and then sharply rise up to  $\sim 4\%$ . The abnormal features of fitting residuals below  
322 302.5 nm shown in Figs. 2 and 6 provide a basis for why we select the lower boundary of the ozone  
323 fitting window as 302.5 nm. The soft calibration is applied before the fitting starts by dividing OMPS  
324 radiances by the derived correction spectrum just at the initial iteration with the assumption that the  
325 systematic biases consistently exist independent of space and time. Figure 7 shows how our  
326 tropospheric ozone retrievals are improved with our soft calibration in comparison with retrievals  
327 shown in Fig. 5.b. The usefulness of our soft calibration implementation is also evaluated through  
328 comparisons of the accuracies of the spectral fitting residuals with and without soft calibration as shown  
329 in Fig. 8. The mean fitting residuals without soft calibration are  $\sim \pm 1\%$  at shorter wavelengths  $< 320$   
330 nm for all latitudes and sky conditions, whereas for longer wavelengths they increase from 0.3 % to  
331 0.5 % with increasing latitudes. Our soft calibration dramatically improves the fitting accuracy for both  
332 clear and cloudy pixels, especially over the tropics and mid-latitude regions; fitting residuals are mostly  
333 within 0.2 % at longer wavelengths  $> 310$  nm. In high latitudes, improvements can be identified, but  
334 large remaining systematic biases can still be found.

### 335 **3.3 Common Mode Correction**

336 In previous section, it is shown that our soft calibration effectively eliminates systematic biases of  
337 measurements relative to VLIDORT simulations for most cases, except for high latitudes/SZAs where  
338 there still exists a distinct wavelength-dependent pattern in fitting residuals because the soft calibration  
339 spectrum is derived only under small SZA conditions. In order to verify and correct such systematic  
340 biases remaining after soft calibration, we characterize spectral fitting residuals at the final iteration  
341 classified into 3 latitude/SZA regimes (southern polar region/SZA>60°, tropical region/ SZA<40°,  
342 northern polar region/ SZA>60°) for each cross-track position and for one day (14<sup>th</sup> or 15<sup>th</sup>) of each  
343 month. The remainder is called the common residual spectrum. Examples of derived common spectra  
344 are presented in Fig. 9 for March and August 2013. The main peak positions of residuals of all common  
345 residual spectra are well matched to each other. The amplitude of tropical residuals is very similar  
346 between two months, whereas the variation of the amplitude at high latitudes seems to be associated  
347 with snow/ice cover and SZA variations such that the amplitude is maximized during the polar winter  
348 season. Applying the common mode correction (CMC) means subtracting the common spectrum with  
349 amplitude determined iteratively along with the rest of state vector components from the measured  
350 spectrum. Fig. 10 compares the fitting residuals at high SZAs for one orbit of data on 02 March 2013  
351 with and without the common mode correction. It is evident that wavelength dependent fitting residuals  
352 are greatly reduced even for the first few wavelengths, with amplitude of spectral residuals reduced  
353 from ~ 1 % to 0.5 %. Moreover, the common mode correction slightly reduces the standard deviations  
354 of residuals. The improvement is seen everywhere as shown in Fig. 11 where RMS of relative fitting  
355 residuals (ratio of fitting residuals to measurements error) is displayed for all individual pixels within  
356 one orbit.

### 357 **3.4 Measurement Error Correction**

358 The measurement error covariance matrix  $S_y$  is one of the essential inputs in an OE based algorithm,  
359 because it significantly affects the stability of retrievals and retrieval sensitivities. OMPS L1B v2.0 data  
360 contain the relative errors of radiance measurements, but these measurement errors (~ 0.04 % @ 320  
361 nm) were too small to regularize our ozone fitting process so that many retrievals fail due to negative  
362 or large positive ozone values as a result of over fitting. Ideally, the measurement errors need to include  
363 not only photon shot noise but also other kinds of random noise errors caused by readout, straylight,  
364 dark current, geophysical pseudo-random noise errors due to sub-pixel variability and motion when

365 taking a measurement, forward model parameter error (random part), and other unknown errors.  
366 However, OMPS measurement errors reported in the L1B only include photon shot noise and read-out  
367 errors, which underestimate the overall measurement error. For this reason, OMI noise floor (NF) errors  
368 instead of OMPS random-noise errors are imposed on our preliminary retrievals, as mentioned in Sect  
369 2.3. However, better signal-to-noise ratios (SNRs) could be expected for OMPS than OMI due to  
370 OMPS's coarser spectral and spatial resolutions, as shown from the improved detection limit of OMPS  
371 H<sub>2</sub>CO retrievals compared to OMI as discussed in Gonzalez Abad et al. (2016). Fig. 11 also implies that  
372 there is room for increasing the Degrees of Freedom for Signals (DFS) to current ozone retrievals by  
373 regularizing them using the improved measurement error instead of using OMI NF; the ideal value of  
374 RMS is one, but our RMS is mostly within 0.4 at low and mid-latitudes. The random-noise component  
375 of measurements could be derived from standard deviations of spectral fitting residuals (Cai et al., 2012;  
376 Liu et al. 2015b). Fig. 12 shows how we derive the measurement errors to improve our retrievals. We  
377 first characterize the minimum measurement errors from fitting residuals under nearly clear-sky  
378 condition at SZAs < 40° and cross-track pixels between 4 and 33; note that no radiometric calibration  
379 is applied to these fitting residuals. The standard deviations of fitting residuals are nearly invariant at  
380 longer wavelengths > 310 nm and show a significant increase from ~ 0.1 % at 310 nm to ~ 0.3 % at 302  
381 nm as plotted with the red dashed line in Fig. 12.a. We eliminate the low-frequency portion of the noises  
382 with a 4<sup>th</sup> order polynomial fit to define the minimum OMPS NF errors as plotted with the red solid  
383 line in Fig. 12.a. The derived NF errors are ~ 2 (1.5-4) times smaller than OMI NF errors above (below)  
384 310 nm and thereby could increase the measurement information in our retrievals. We impose the  
385 minimum NF errors as a measurement constraint in our algorithm when SZAs are smaller than ~ 20°,  
386 whereas they are multiplied by a SNR scaling factor to increase measurement errors as a function of  
387 SZAs. Figure 12.b shows an example of how derived measurement errors increase with SZA at the  
388 boundary wavelengths of the ozone fitting window, with errors from 0.24 % to 0.45 % for 302.5 nm  
389 and from 0.097 % to 0.19 % for 340 nm.

390 Figure 13 shows the effect of using the derived NF errors on our retrievals. The RMS of fitting  
391 residuals increases from 0.2-0.4 to 0.4-0.8 in swath lines 50-350, where SZAs are within ~ 60°, due to  
392 SNR increases, whereas the average fitting residuals slightly improves by 0.015 %. Using the new NF  
393 errors slightly increases the number of iterations; one or more iterations are required for ~ 24 % of the  
394 total retrieved pixels and hence our fitting process converges mostly within 3-4 times, except for thick  
395 clouds where the number of iterations increases to 6. Using the derived NF errors significantly increases  
396 the retrieval information content. Both stratospheric and tropospheric DFSs are improved by 0.2-0.4  
397 under mild SZAs and by up to 0.2 under high SZAs as shown in Fig. 14, so that tropospheric ozone

398 retrievals demonstrate  $\sim 1$  DFS in low/mid latitudes, which is similar to OMI retrievals (Liu et al.,  
399 2010a). Fig 15.a shows the retrieved tropospheric ozone column distribution with two radiometric  
400 calibrations (soft, CMC) and OMPS NF errors. Compared to Fig 7.b without CMC and OMI NF errors,  
401 the cross-track dependent noises over the polar region are smoothed due to CMC and the columns are  
402 enhanced in the tropics and the northern mid-latitudes due to OMPS NF errors. Successful tropospheric  
403 retrievals typically require better than 0.2-0.3 % fitting accuracy between measured and modeled  
404 radiances in the Huggins band (310-340 nm) (Munro et al., 1998). Our fitting algorithm meets this  
405 requirement after carefully applying empirical calibrations as shown in Fig 15.b; the average fitting  
406 residuals are within 0.1 % for moderate SZAs, with insignificant dependence on cross-track position.

#### 407 **4. Conclusions**

408 The OMI ozone profile algorithm has been adapted and modified to retrieve tropospheric ozone and  
409 ozone profiles from OMPS-NM L1B 2.0 product. To verify the best knowledge of OMPS instrument  
410 slit functions, we evaluate OMPS preflight measured slit functions and analytical slit functions  
411 assuming standard and super Gaussian distributions through cross-correlation using a high-resolution  
412 solar reference spectrum. We also adjust preflight measured slit functions to post-launch OMPS  
413 measurements by broadening/squeezing them by up to 4%, which slightly improves the fitting residuals  
414 at nadir cross-track pixels, but by up to 0.18% (e.g., from 0.75% to 0.6% at the first cross-track position)  
415 at edge pixels. The super Gaussian slit functions better represent OMPS irradiances than the standard  
416 Gaussian and even the preflight measured slit functions, but the fitting residuals of radiances with  
417 different slit functions show insignificant differences. OMPS measured slit functions are finally  
418 implemented in our OMPS ozone fitting retrievals because they take account of the slight dependence  
419 of slit functions on wavelengths.

420 We perform two kinds of radiometric calibrations to eliminate the systematic components of fitting  
421 residuals. First, we apply “soft calibration” to OMPS radiance before retrievals. This correction  
422 spectrum is derived as a function of wavelength and cross-track position by averaging the ratio of  
423 measured radiances to simulated radiances using collocated OMI ozone profile retrievals in the tropics  
424 under nearly clear-sky conditions for 25 days of May 2013. Applying soft calibration to OMPS radiance  
425 dramatically improves the spectral fitting residuals, especially under low to moderate SZA. The  
426 amplitude of fitting residuals decreases from 1 % to 0.2 %. Therefore, the significant cross-track striping  
427 pattern shown in preliminary OMPS tropospheric ozone retrievals is mostly eliminated. Second, the  
428 CMC is implemented to compensate fitting residuals uncorrected by soft calibration, especially for high

429 SZA retrievals. This correction spectrum is derived as functions of wavelength and cross-track position  
430 by averaging one day's fitting residuals over the tropics and northern/southern high latitude regions,  
431 respectively. The amplitude of the correction spectrum is iteratively and simultaneously adjusted with  
432 ozone. It is found that the amplitude of the fitting residuals decreases by a factor of 2 due to the CMC  
433 over high latitudes.

434 Our preliminary algorithm uses OMI NF errors to represent measurement constraints because OMPS  
435 L1B random-noise errors are too tight to stabilize retrievals. However, we found that OMI NF errors  
436 cannot sufficiently constrain our OMPS retrievals, indicating that there is room to increase the retrieval  
437 sensitivity to measurement information by improving measurement constraints. Therefore, we derive  
438 the minimum NF error corresponding to standard deviations of spectral fitting residuals over the tropics.  
439 The derived minimum NF error is  $\sim 0.097\%$  in 310-340 nm and increases to  $\sim 0.24\%$  at 302.5 nm,  
440 which is smaller than OMI error by a factor of 1.5-4 below 310 nm and 2 above. We apply this OMPS  
441 NF error at SZAs  $< \sim 20^\circ$  and those multiplied by a SNR scaling factor to take into account the  
442 decreasing SNR with increasing SZA at SZAs  $> \sim 20^\circ$ ; at SZA =  $90^\circ$  errors becomes 0.45 % at 302.5  
443 nm and 0.19 % at 340 nm. Using OMPS NF errors as a retrieval constraint slightly improves the fitting  
444 residuals, by 0.015 % on average, and both stratospheric and tropospheric ozone retrieval sensitivity  
445 (DFS increases by 0.2-0.4), but requires 1 or more additional iterations for convergence. In this study,  
446 we meet the requirement to achieve successful tropospheric ozone retrievals in terms of DFS ( $> 1$ ) and  
447 fitting residuals ( $< 0.2$ - $0.3\%$ ) with empirical calibrations optimized to OMPS L1B measurements. In  
448 future work, we will characterize OMPS ozone profile retrievals, present error analysis, and validate  
449 retrievals using a reference dataset, to verify that the quality of OMPS ozone retrievals is adequate for  
450 scientific use.

451

## 452 **Acknowledgements**

453 We acknowledge the OMI and OMPS science teams for providing their satellite data and Glen Jaross  
454 for providing useful comments regarding OMPS level 1B v2.0 data. We thank Alexander Vasilkov for  
455 allowing the OMPS cloud product to be used in this study. Research at Pusan National University by J.  
456 Bak and J.H. Kim was financially supported by the 2016 Post-Doc. Development Program of Pusan  
457 National University. Research at the Smithsonian Astrophysical Observatory by X. Liu, K. Chance, and  
458 K. Sun was funded by NASA Aura science team program (NNX14AF16G) and the Smithsonian  
459 Institution. K. Yang was funded by NASA Suomi NPP science team program (NNX14AR20A).

## 460 **References**

- 461 Bak, J., Kim, J. H., Liu, X., Chance, K., and Kim, J.: Evaluation of ozone profile and tropospheric ozone  
462 retrievals from GEMS and OMI spectra, *Atmos. Meas. Tech.*, 6, 239–249, doi:10.5194/amt-6-239-  
463 2013, 2013a.
- 464 Bak, J., Libaku, X., Wei, J. C., Pan, L. L., Chance, K., and Kim, J. H.: Improvement of OMI ozone  
465 profile retrievals in the upper troposphere and lower stratosphere by the use of a tropopause-based  
466 ozone profile climatology, *Atmos. Meas. Tech.*, 6, 2239–2254, doi:10.5194/amt-6-2239-2013,  
467 2013b.
- 468 Beirle, S., Lampel, J., Lerot, C., Sihler, H., and Wagner, T.: Parameterizing the instrumental spectral  
469 response function and its changes by a super-Gaussian and its derivatives, *Atmos. Meas. Tech.*, 10,  
470 581–598, <https://doi.org/10.5194/amt-10-581-2017>, 2017.
- 471 Bhartia, P. K. and Wellemeyer, C.: TOMS-V8 total O<sub>3</sub> algorithm, in: *OMI Algorithm Theoretical Basis*  
472 *Document, Vol. II, OMI Ozone Products*, edited by: Bhartia, P. K., 15–31, NASA Goddard Space  
473 Flight Cent., Greenbelt, MD, 2002.
- 474 Bovensmann, H., Burrows, J. P., Buchwitz, M., Frerick, J., Noel, S., Rozanov, V. V., Chance, K. V.,  
475 and Goede, A. P. H.: *SCIAMACHY: Mission objectives and measurement modes*, *J. Atmos. Sci.*,  
476 56, 127–150, doi:10.1175/1520-0469(1999)056<0127:SMOAMM>2.0.CO;2, 1999.
- 477 Brion, J., Chakir, A., Daumont, D., and Malicet, J.: High-resolution laboratory absorption cross section  
478 of O<sub>3</sub>. Temperature effect, *Chem. Phys. Lett.*, 213, 610–612, 1993.
- 479 Cai, Z., Liu, Y., Liu, X., Chance, K., Nowlan, C. R., Lang, R., Munro, R., and Suleiman, R.: ,  
480 Characterization and correction of Global Ozone Monitoring Experiment 2 ultraviolet  
481 measurements and application to ozone profile retrievals, *J. Geophys. Res.*, 117, D07305,  
482 doi:10.1029/2011JD017096, 2012.
- 483 Caspar, C. and Chance, K.: GOME wavelength calibration using solar and atmospheric spectra, Third  
484 ERS Symposium on Space at the Service of our Environment, Florence, Italy, 14–21 March, 1997.
- 485 Chance, K. and Kurucz, R. L.: An improved high-resolution solar reference spectrum for earth's  
486 atmosphere measurements in the ultraviolet, visible, and near infrared, *J. Quant. Spectrosc. Ra.*, 111,  
487 1289–1295, doi:10.1016/j.jqsrt.2010.01.036, 2010.
- 488 Chance, K., Liu, X., Suleiman, R. M., Flittner, D. E., Al-Saadi, J., and Janz, S. J.: Tropospheric  
489 emissions: monitoring of pollution (TEMPO), *Proc. SPIE 8866, Earth Observing Systems XVIII*,  
490 8866, 88660D-1–88660D-16, doi:10.1117/12.2024479, 2013.
- 491 Dirksen, R., Dobber, M., Voors, R., and Levelt, P.: Prelaunch characterization of the Ozone Monitoring  
492 Instrument transfer function in the spectral domain, *Appl. Opt.*, 45, 3972–3981,  
493 10.1364/ao.45.003972, 2006.
- 494 European Space Agency: *The GOME Users Manual*, ESA Publ. SP-1182, Publ. Div., Eur. 488 Space  
495 Res. and Technol. Cent., Noordwijk, The Netherlands, 1995.



496 European Organisation for the Exploitation of Meteorological Satellites (EUMETSAT) : GOME-2  
497 level 1 Product Generation Specification, Rep. EPS.SYS.SPE.990011, Darmstadt, Germany, 2006.

498 Flynn, L., Long, C., Wu, X., Evans, R., Beck, C. T., Petropavlovskikh, I., McConville, G., Yu, W.,  
499 Zhang, Z., Niu, J., Beach, E., Hao, Y., Pan, C., Sen, B., Novicki, M., Zhou, S., and Seftor, C. :  
500 Performance of the Ozone Mapping and Profiler Suite (OMPS) products, *J. Geophys. Res. Atmos.*,  
501 119, 6181–6195, doi:10.1002/2013JD020467, 2014.

502 G. González Abad, A. Vasilkov, C. Seftor, X. Liu, and K. Chance: Smithsonian Astrophysical  
503 Observatory Ozone Mapping and Profiler Suite (SAO OMPS) formaldehyde retrieval, *Atmos. Meas.*  
504 *Tech.*, 9, 2797-2812, 2016.

505 Huang, G., Liu, X., Chance, K., Yang, K. et al.: Validation of 10-year SAO OMI Ozone Profile  
506 (PROFOZ) Product Using Ozone Sonde Observations, *Atmos. Meas. Tech. Discuss.*,  
507 doi:10.5194/amt-2017-15, 2017a.

508 Huang, G., Liu, X., Chance, K., Yang, K., and Cai, Z.: Validation of 10-year SAO OMI Ozone  
509 Profile (PROFOZ) Product Using Aura MLS Measurements, *Atmos. Meas. Tech. Discuss.*,  
510 <https://doi.org/10.5194/amt-2017-92>, in review, 2017b

511 Hörmann, C., Sihler, H., Beirle, S., Penning de Vries, M., Platt, U., and Wagner, T.: Seasonal variation  
512 of tropospheric bromine monoxide over the Rann of Kutch salt marsh seen from space, *Atmos.*  
513 *Chem. Phys.*, 16, 13015-13034, doi:10.5194/acp-16-13015-2016, 2016.

514 Jaross, G.: OMPS/NPP L1B NM Radiance EV Calibrated Geolocated Swath Orbital V2, Goddard Earth  
515 Sciences Data and Information Services Center (GES DISC), Greenbelt, MD, USA, accessed July  
516 20, 2017, doi:10.5067/DL081SQY7C89, 2017

517 Kleipool, Q. L., Dobber, M. R., de Haan, J. F., and Levelt, P. F.: Earth surface reflectance climatology  
518 from 3 years of OMI data, *J. Geophys. Res.*, 113, D18308, doi: 10.1029/2008JD010290, 2008.

519 Kroon, M., de Haan, J. F., Veeffkind, J. P., Froidevaux, L., Wang, R., Kivi, R., and Hakkarainen, J. J.:  
520 Validation of operational ozone profiles from the Ozone Monitoring Instrument, *J. Geophys. Res.*,  
521 116, D18305, doi: 10.1029/2010JD015100, 2011.

522 Kurosu, T.P., Chance, K., and Sioris, C.E. : "Preliminary results for HCHO and BrO from the EOS-  
523 Aura Ozone Monitoring Instrument", in *Passive Optical Remote Sensing of the Atmosphere and*  
524 *Clouds IV*, Proc. of SPIE Vol. 5652 , doi: 10.1117/12.578606, 2004.

525 Levelt, P. F., van den Oord, G. H. J., Dobber, M. R., Malkki, A., Visser, H., de Vries, J., Stammes, P.,  
526 Lundell, J. O. V., and Saari, H.: The Ozone Monitoring Instrument, *IEEE Trans. Geosci. Remote*  
527 *Sens.*, 44(5), 1093–1101, doi:10.1109/TGRS.2006.872333, 2006.

528 Liu, X., Chance, K., Sioris, C. E., Spurr, R. J. D., Kurosu, T. P., Martin, R. V., and Newchurch, M. J.:  
529 Ozone profile and tropospheric ozone retrievals from Global Ozone Monitoring Experiment:

530 algorithm description and validation, *J. Geophys. Res.*, 110, D20307, doi: 10.1029/2005JD006240,  
531 2005.

532 Liu, X., Chance, K., Sioris, C.E, and Kurosu, T.P: Impact of using different ozone cross sections on  
533 ozone profile retrievals from GOME ultraviolet measurements. *Atmos. Chem. Phys.*, 7, 3571-3578,  
534 2007.

535 Liu, X., Bhartia, P.K, Chance, K, Spurr, R.J.D., and Kurosu, T.P.: Ozone profile retrievals from the  
536 ozone monitoring instrument. *Atmos. Chem. Phys.*, 10, 2521–2537, 2010a.

537 Liu, C., Liu, X., Kowalewski, M.G., Janz, S.J., González Abad, G., Pickering, K.E., Chance, K., and  
538 Lamsal, L.N.: Characterization and verification of ACAM slit functions for trace gas retrievals  
539 during the 2011 DISCOVER-AQ flight campaign, *Atmos. Meas. Tech.*, 8, 751-759,  
540 doi:10.5194/amt-8-751-2015, 2015a.

541 Liu, C., Liu, X., Kowalewski, M.G., Janz, S.J., González Abad, G., Pickering, K.E., Chance, K., and  
542 Lamsal, L.N.: Analysis of ACAM Data for Trace Gas Retrievals during the 2011 DISCOVER-AQ  
543 Campaign, , *J. Spectroscopy*, ID827160, doi:10.1155/2015/827160, 2015, 827160, 2015b.

544 Munro, R., Lang, R., Klaes, D., Poli, G., Retscher, C., Lindstrot, R., Huckle, R., Lacan, A., Grzegorski,  
545 M., Holdak, A., Kokhanovsky, A., Livschitz, J., and Eisinger, M.: The GOME-2 instrument on the  
546 MetOp series of satellites: instrument design, calibration, and level 1 data processing – an overview,  
547 *Atmos. Meas. Tech.*, 9, 1279-1301, doi:10.5194/amt-9-1279-2016, 2016.

548 Nowlan, C. R., Liu, X., Chance, K., Cai, Z., Kurosu, T. P., Lee, C., and Martin, R. V.: Retrievals of  
549 sulfur dioxide from the global ozone monitoring experiment 2 (GOME-2) using an optimal  
550 estimation approach: algorithm and initial validation, *J. Geophys. Res.-Atmos.*, 116, D18301,  
551 doi:10.1029/2011JD015808, 2011.

552 Rodgers, C. D.: *Inverse Methods for Atmospheric Sounding: Theory and Practice*, World Scientific  
553 Publishing, Singapore, 2000.

554 Pittman, J.V., Pan, L.L., Wei, J.C., Irion, F.W., Liu, X., Maddy, E.S., Barnet, C.D., Chance, K., and  
555 Gao, R.-S.: Evaluation of AIRS, IASI, and OMI ozone profile retrievals in the extratropical  
556 tropopause region using in situ aircraft measurements, *J. Geophys. Res.*, 114, D24109,  
557 doi:10.1029/2009JD012493, 2009.

558 Schenkeveld, V. M. E., Jaross, G., Marchenko, S., Haffner, D., Kleipool, Q. L., Rozemeijer, N. C.,  
559 Veefkind, J. P., and Levelt, P. F.: In-flight performance of the Ozone Monitoring Instrument, *Atmos.*  
560 *Meas. Tech.*, 10, 1957-1986, <https://doi.org/10.5194/amt-10-1957-2017>, 2017.

561 Seftor, C. J., Jaross, G., Kowitt, M., Haken, M., Li, J., and Flynn, L. E.: Postlaunch performance of the  
562 Suomi National Polar orbiting Partnership Ozone Mapping and Profiler Suite (OMPS) nadir sensors,  
563 *J. Geophys. Res. Atmos.*, 119, doi: 10.1002/2013JD020472., 2014.

564 Seftor, C. J. and Jaross, G.: NMEV-L1B Data Release Notes,  
565 [https://ozoneaq.gsfc.nasa.gov/omps/media/docs/NMEV-L1B\\_Release\\_Notes.pdf](https://ozoneaq.gsfc.nasa.gov/omps/media/docs/NMEV-L1B_Release_Notes.pdf), accessed 20 July  
566 2017.

567 Sioris, C. E., and Evans, W. F. J.: Impact of rotational Raman scattering in the O2 A band, *Geophys.*  
568 *Res. Lett.*, 27(24), 4085–4088, 2000.

569 Spurr, R. J.: VLIDORT: A linearized pseudo-spherical vector discrete ordinate radiative transfer code  
570 for forward model and retrieval studies in multilayer multiple scattering media, *J. Quant. Spectrosc.*  
571 *Ra.*, 102, 316–342, doi:10.1016/j.jqsrt.2006.05.005, 2006.

572 Spurr, R. J. D.: Linearized pseudo-spherical scalar and vector discrete ordinate radiative transfer models  
573 for use in remote sensing retrieval problems, in: *Light Scattering Reviews*, edited by: Kokhanovsky,  
574 A., Springer, New York, 2008.

575 Sun, K., Liu, X., Nowlan, C. R., Cai, Z., Chance, K., Frankenberg, C., Lee, R. A. M., Pollock, R.,  
576 Rosenberg, R., and Crisp, D.: Characterization of the OCO-2 instrument line shape functions using  
577 on-orbit solar measurements, *Atmos. Meas. Tech.*, 10, 939-953, [https://doi.org/10.5194/amt-10-](https://doi.org/10.5194/amt-10-939-2017)  
578 [939-2017](https://doi.org/10.5194/amt-10-939-2017), 2017a. Sun, K., Liu, X., Huang, G., González Abad, G., Cai, Z., Chance, K., and Yang,  
579 K.: Deriving the slit functions from OMI solar observations and its implications for ozone-profile  
580 retrieval, *Atmos. Meas. Tech. Discuss.*, <https://doi.org/10.5194/amt-2017-129>, in review, 2017b.

581 Vasilkov, A., Joiner, J., and Seftor, C.: First results from a rotational Raman scattering cloud algorithm  
582 applied to the Suomi National Polar-orbiting Partnership (NPP) Ozone Mapping and Profiler Suite  
583 (OMPS) Nadir Mapper, *Atmos. Meas. Tech.*, 7, 2897-2906, doi: 10.5194/amt-7-2897-2014, 2014.

584 Veefkind, J. P., Aben, I., McMullan, K., Förster, H., de Vries, J., Otter, G., Claas, J., Eskes, H. J., de  
585 Haan, J. F., Kleipool, Q., van Weele, M., Hasekamp, O., Hoogeveen, R., Landgraf, J., Snel, R., Tol,  
586 P., Ingmann, P., Voors, R., Kruizinga, B., Vink, R., Visser, H. and Levelt, P. F.: TROPOMI on the  
587 ESA Sentinel-5 Precursor: A GMES mission for global observations of the atmospheric  
588 composition for climate, air quality and ozone layer applications, *Remote Sensing of Environment*,  
589 120(0), 70–83, doi:10.1016/j.rse.2011.09.027, 2012.

590 Yang, K., Dickerson, R.R. ,Carn, S.A. , Ge, C. , and Wang, J.: First observations of SO<sub>2</sub> from the  
591 satellite Suomi NPP OMPS: Widespread air pollution events over China, *GRL.*,  
592 doi:10.1002/grl.50952, 2013.

593 Yang, K., Carn, S. A., Ge, C., Wang, J., and Dickerson, R. R. : Advancing measurements of tropospheric  
594 NO<sub>2</sub> from space: New algorithm and first global results from OMPS, *Geophys. Res. Lett.*, 41, doi:  
595 10.1002/2014GL060136, 2014.

596 Zoogman, P. et al.: Tropospheric Emission: Monitoring of Pollution (TEMPO), *J. Quant. Spectrosc. &*  
597 *Radiat. Transfer*, 186, 17-39, doi:org/10.1016/j.jqsrt.2016.05.008, 2017.

598  
599  
600  
601  
602  
603  
604  
605

606

607 **Table1. Surface and atmospheric input parameters and cross section data used in forward model**  
608 **calculations.**

Forward model Parameters	Data Source
O <sub>3</sub> cross sections	Brion et al. (1993)
Ozone Profile <sup>a</sup>	OMI ozone profiles from Liu et al. (2010)
Temperature profile, surface/tropopause pressure	Daily National Centers for Environmental Prediction (NCEP) final (FNL) operational global analysis data ( <a href="http://rda.ucar.edu/datasets/ds083.2/">http://rda.ucar.edu/datasets/ds083.2/</a> )
Surface albedo	OMI surface climatology (Kleipool et al., 2008)
Cloud fraction	Derived at 347 nm
Cloud-top pressure <sup>b</sup>	OMPS Cloud Optical Centroid Pressures (OCPs) (Vasilkov et al., 2014)

609 <sup>a</sup>OMI ozone profiles retrieved at 48×52 km<sup>2</sup> with spatial coadding and then interpolated to 5° × 5° to fill  
610 bad pixels.

611 <sup>b</sup>OCPs retrieved from OMPS-NM L1B v1.0 measurements using a rotational Raman scattering cloud  
612 algorithm.

613

614

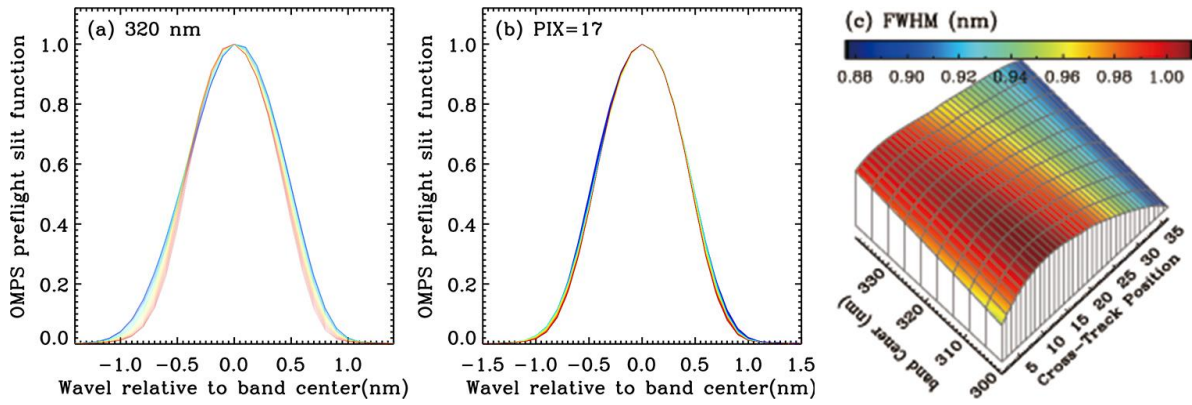
615

616

617

618

619



620

621 **Figure 1. (a) OMPS preflight slit function at 320 nm band center, with colors representing different cross-**  
 622 **track positions from 1 (blue) to 36 (red). (b) Same as (a), but for the 17<sup>th</sup> cross-track position, with colors**  
 623 **representing different wavelengths from 300 nm (blue) to 340 nm (red). (c) Full Width at Half Maximum**  
 624 **(FWHM) in nm as functions of cross-track positions (x-axis) and band center wavelengths (y-axis) ranging**  
 625 **from 300 to 340 nm.**

626

627

628

629

630

631

632

633

634

635

636

637

638

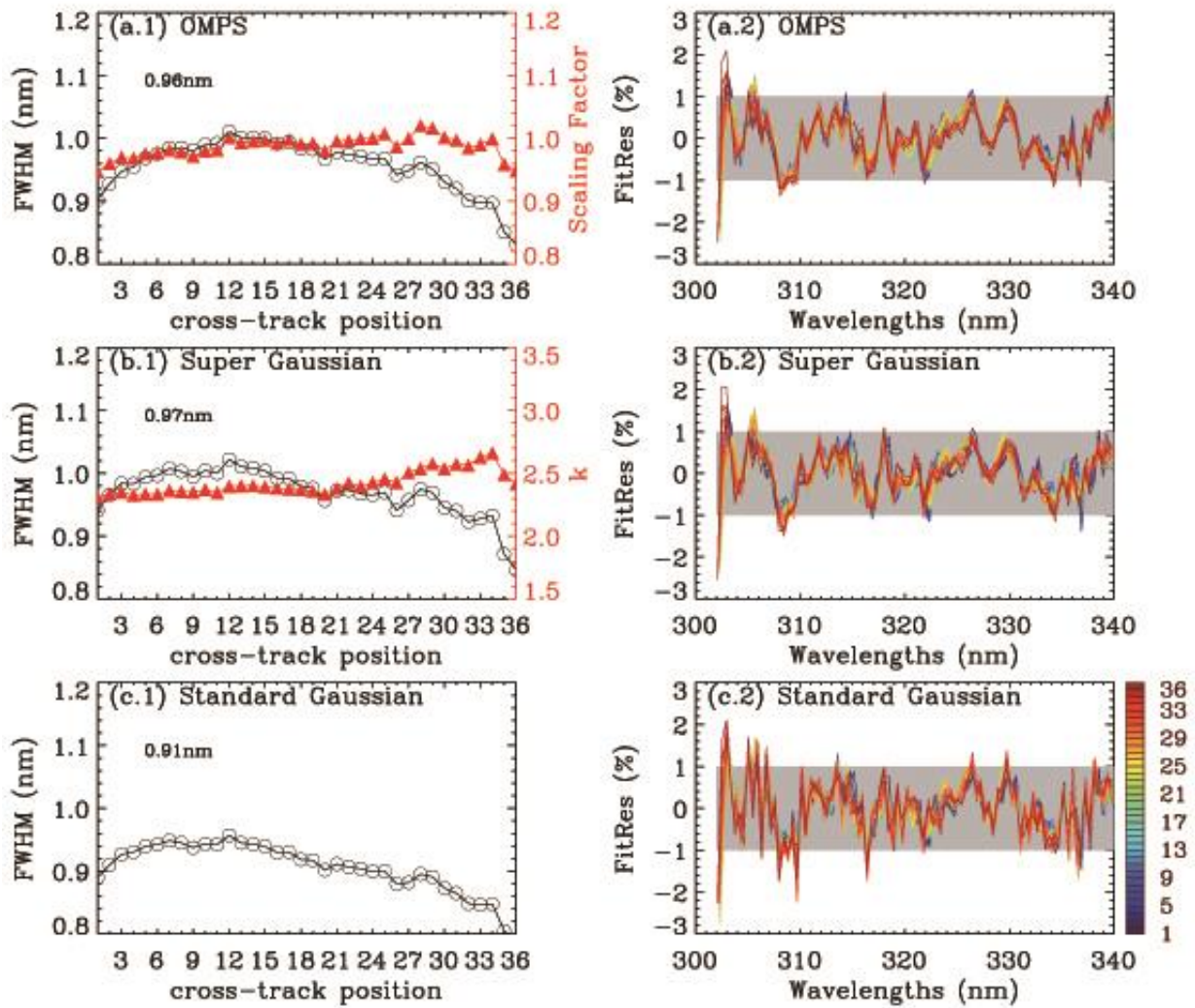
639

640

641

642

643



645

646 Figure 2. (Left) Slit function parameters as a function of cross-track position (1<sup>th</sup>-36<sup>th</sup>) for three different  
 647 slit functions from OMPS irradiance measurements (302-340 nm) for orbit 7132 on 14 March 2013. The  
 648 legends represent the FWHM averaged over all spectral pixels. (Right) The corresponding relative fitting  
 649 residuals between measured and simulated irradiance spectra.

650

651

652

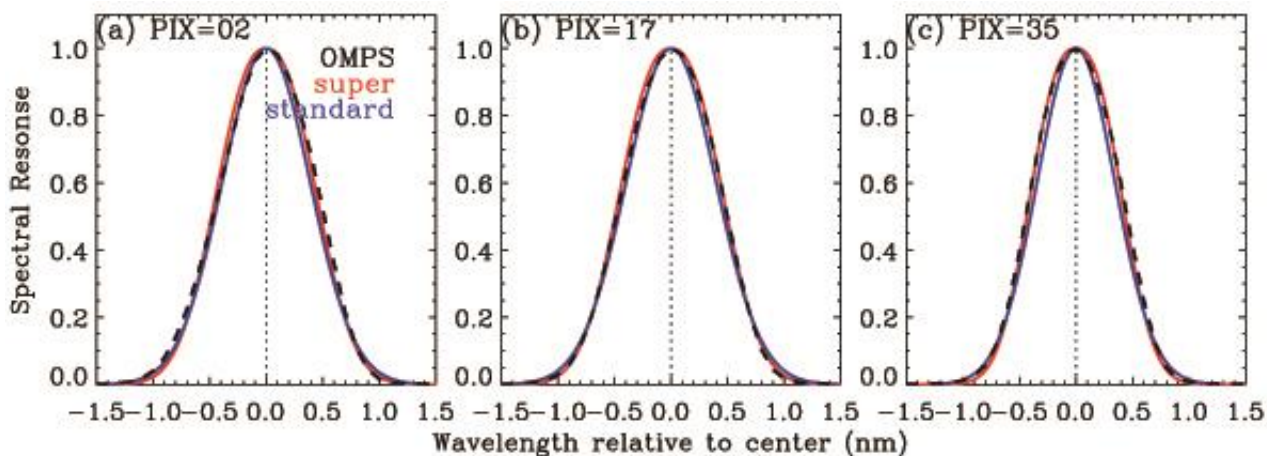
653

654

655

656

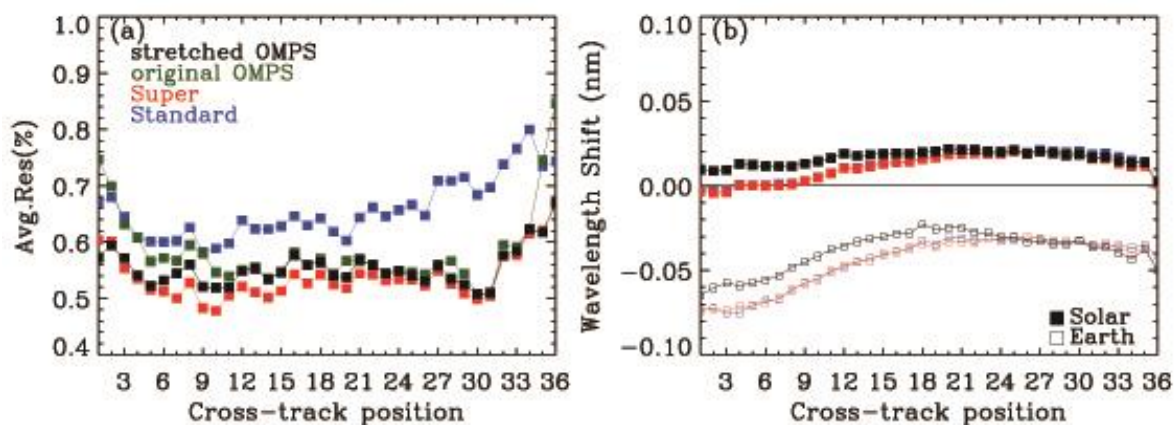
657



658

659 Figure 3. Comparison of OMPS measured slit measurements (black) and derived slit functions assuming a  
660 standard Gaussian (red) and super Gaussian (blue) for orbit 7132.

661



662

663 Figure 4. Same as Fig. 2, but for (a) average fitting residuals (%) as a function of cross-track positions. The  
664 green line represents the fitting residuals with measured OMPS slit functions without fitting a scaling factor.  
665 (b) Wavelength shifts between OMPS irradiance and reference spectrum (filled symbols) and between  
666 OMPS radiance at the middle swath line and reference spectrum (opened symbols).

667

668

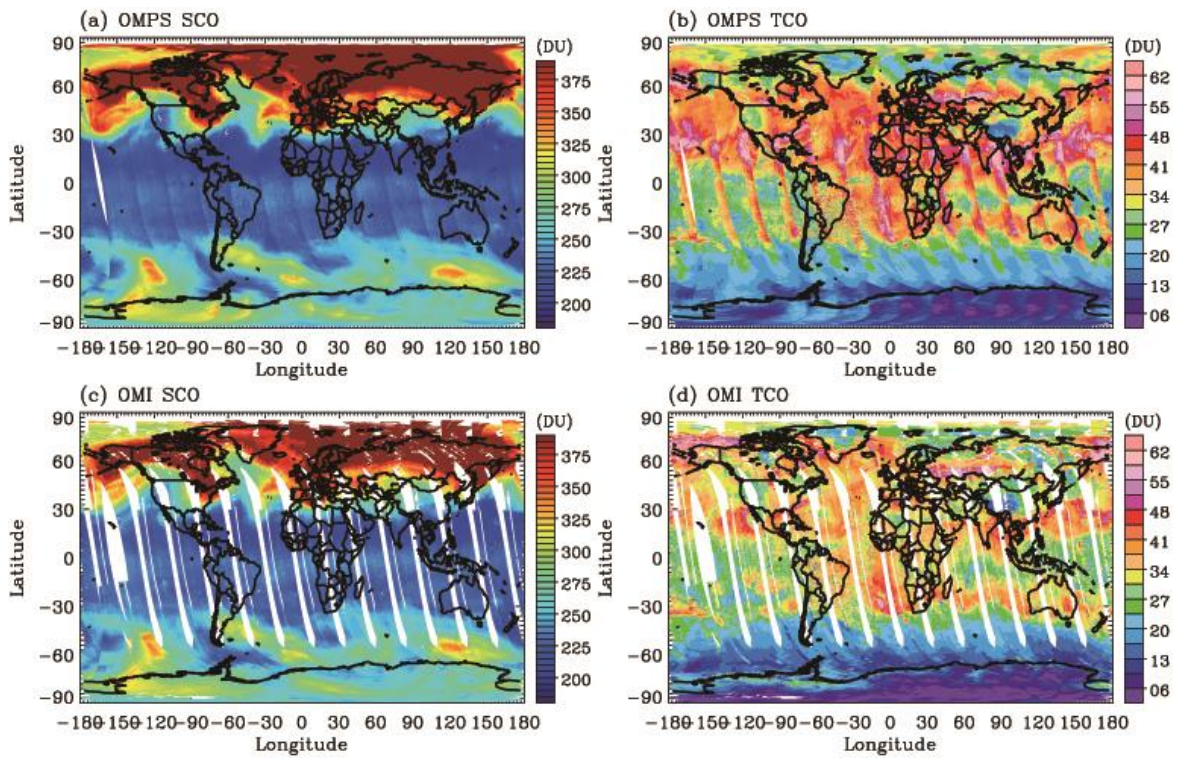
669

670

671



672  
673



674

675 **Figure 5. Maps of stratospheric and tropospheric ozone column on 14 March 2013, retrieved from OMPS**  
676 **(top) without any correction and OMI (bottom) measurements, respectively.**

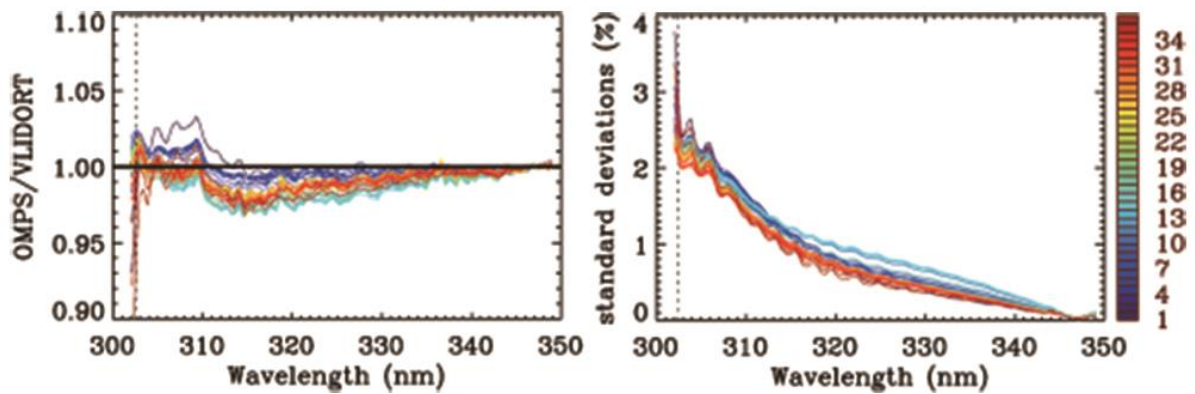
677

678

679

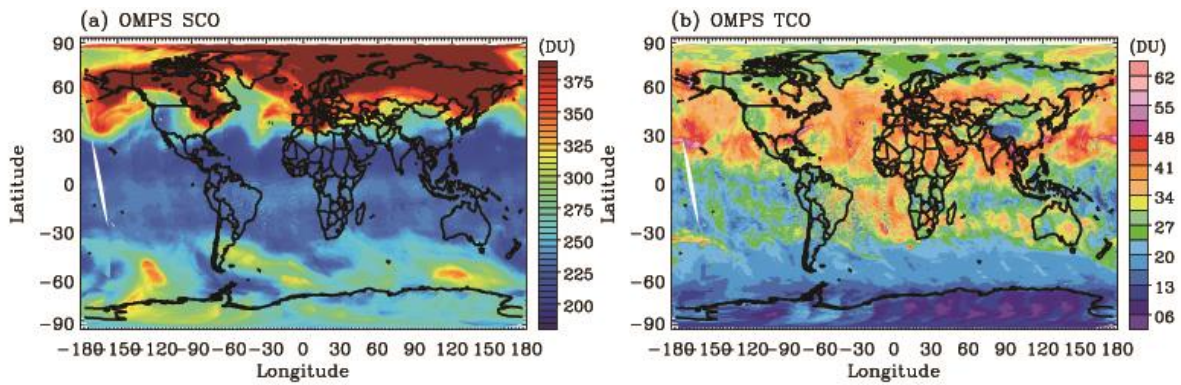
680





681

682 Figure 6. (a) Soft calibration spectrum derived from OMPS measured to simulated radiance ratio at initial  
 683 iteration, as a function of wavelength ranging from 302 nm to 350 nm. The vertical dotted line indicates  
 684 302.5 nm. OMPS data used in this calculation is limited to tropical clear-sky conditions (latitude  $< \pm 15^\circ$ ,  
 685 cloud fraction  $< 0.1$ , surface reflectivity  $< 0.1$ ) for 25 days between 1 March 2013 and 25 March 2013.  
 686 Forward model inputs listed in Table 1 are used for OMPS simulations. (b) Standard deviations of fitting  
 687 residuals. Different colors represent various cross-track positions.



688

689 Figure 7. Same as Figure 5 (a) and (b), but for OMPS ozone retrievals with soft calibration.

690

691

692

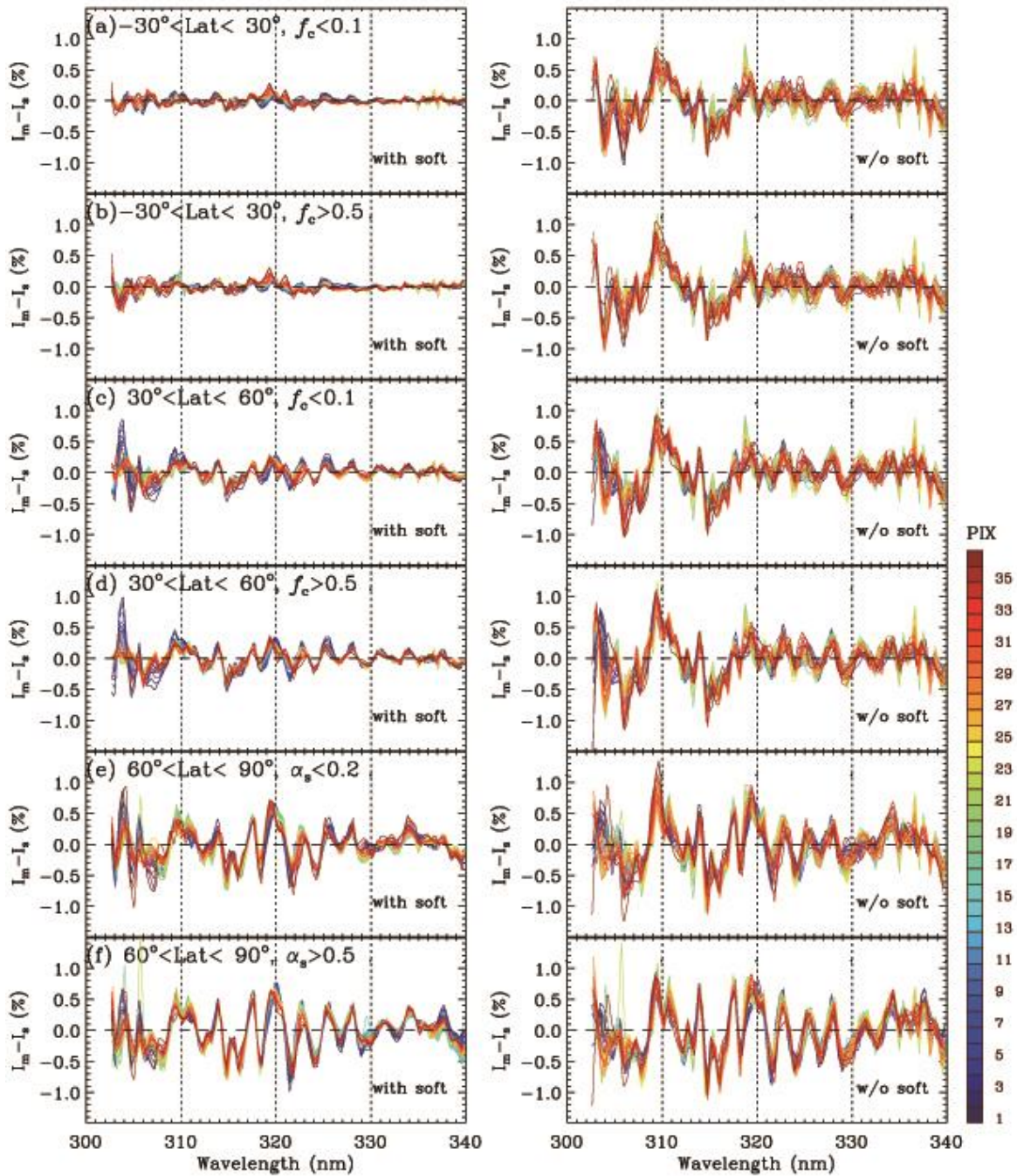
693

694

695

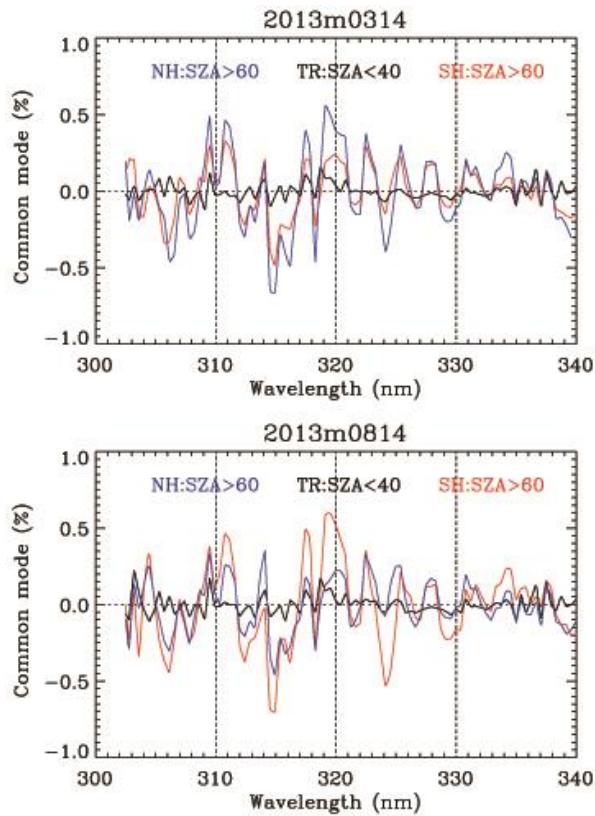
696

697



698

699 **Figure 8.** Comparison of fitting residuals on 14 March 2013 with (left) and without (right) soft calibration  
 700 for 6 cases: (a-b) Tropics and (c-d) mid-latitudes each for clear sky (effective cloud fraction,  $f_c < 0.1$ ) and  
 701 cloudy ( $f_c > 0.5$ ) conditions and (e-f) high-latitudes for snow-free and snow-covered surface conditions.  
 702 Different colors represent different cross-track positions.



703

704 **Figure 9. Common mode spectra derived from final fitting residuals at the 17<sup>th</sup> cross-track position using**  
 705 **one day of measurements in March (upper) and August (lower), respectively. Note that tropical residuals**  
 706 **are derived from nearly clear-sky conditions where SZA < 40°, cloud fraction < 0.1, and surface albedo <**  
 707 **0.1. No special data screening is applied for polar residual spectra, except for SZA > 60°.**

708

709

710

711

712

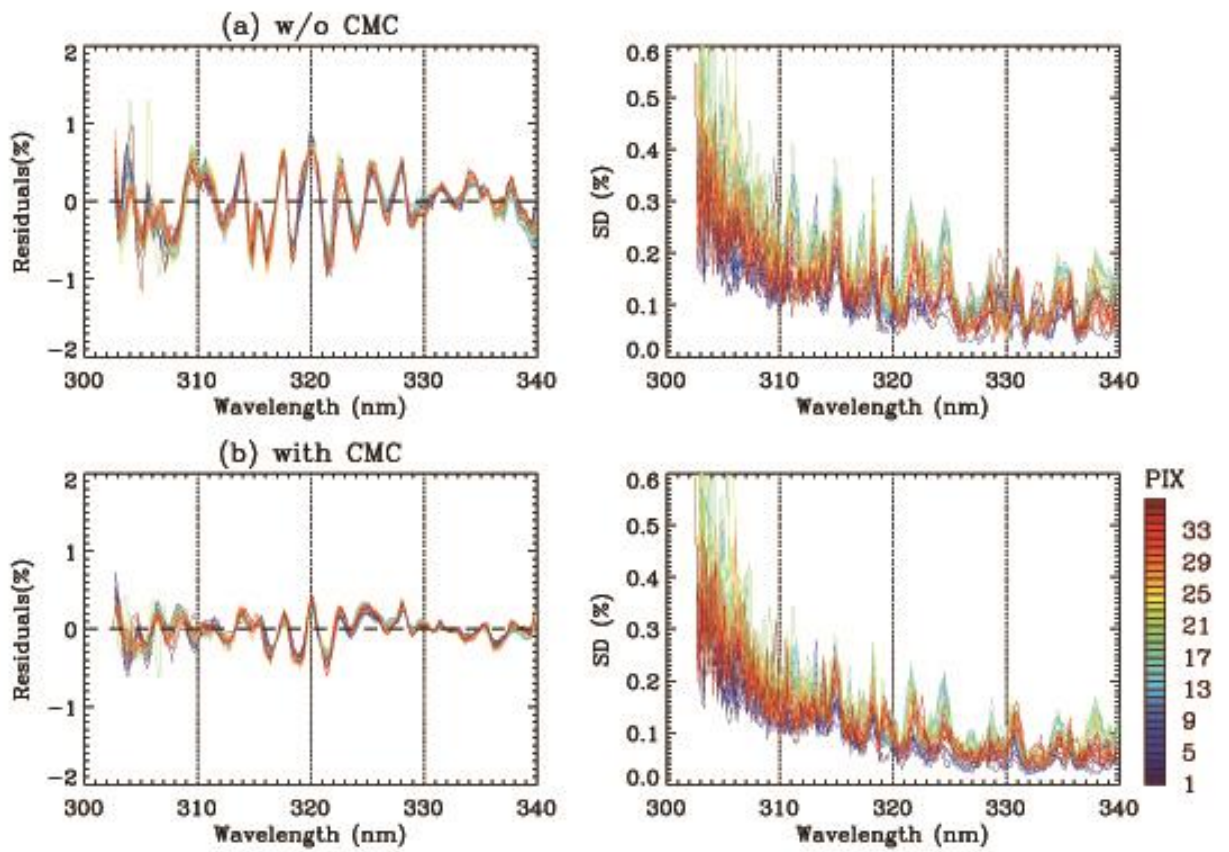
713

714

715

716



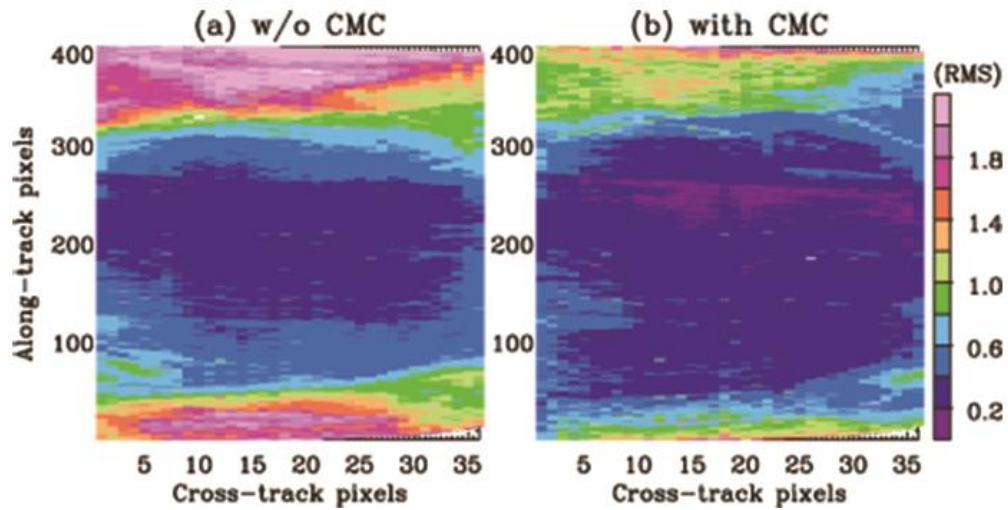


717  
 718 **Figure 10. Comparisons of mean fitting residuals (%) and its standard deviations (%) for latitude > 60°, with different cross-track positions in different colors for one orbit data (6962) on 02 March 2013, without**  
 719 **(a) and with (b) common mode correction.**  
 720

721

722

723

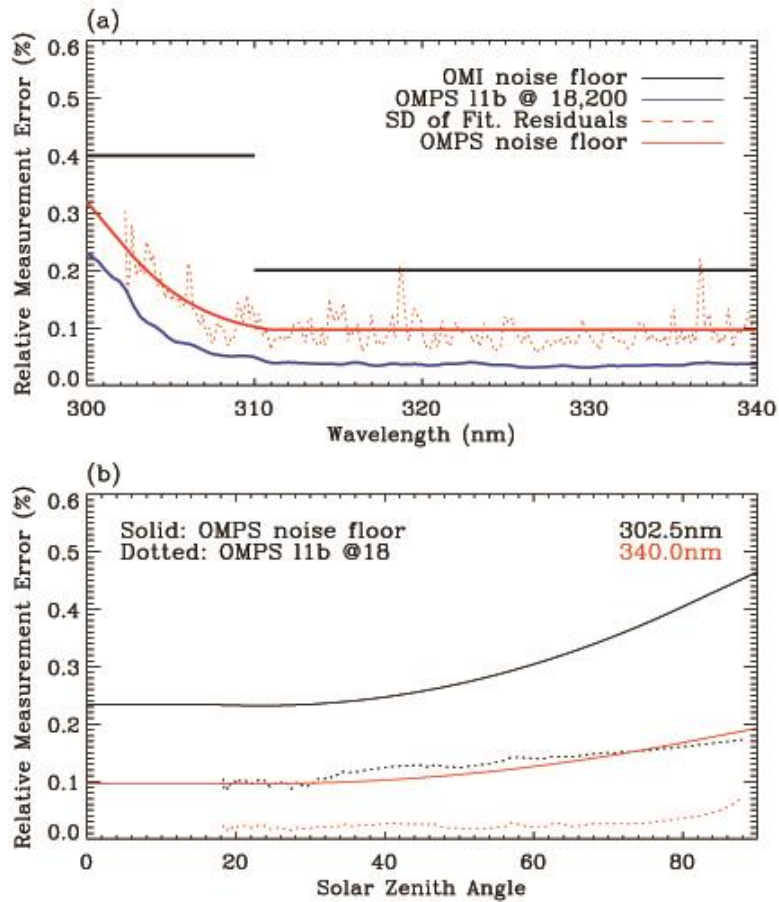


724

725 Figure 11. Same as Figure 10, but for Root Mean Square (RMS) of fitting residuals relative to the

726 measurement errors as functions of along- and cross-track pixels. The RMS is defined as  $\sqrt{\frac{1}{n} \sum_i^n \left( \frac{Y-R}{S_y^{1/2}} \right)^2}$ .

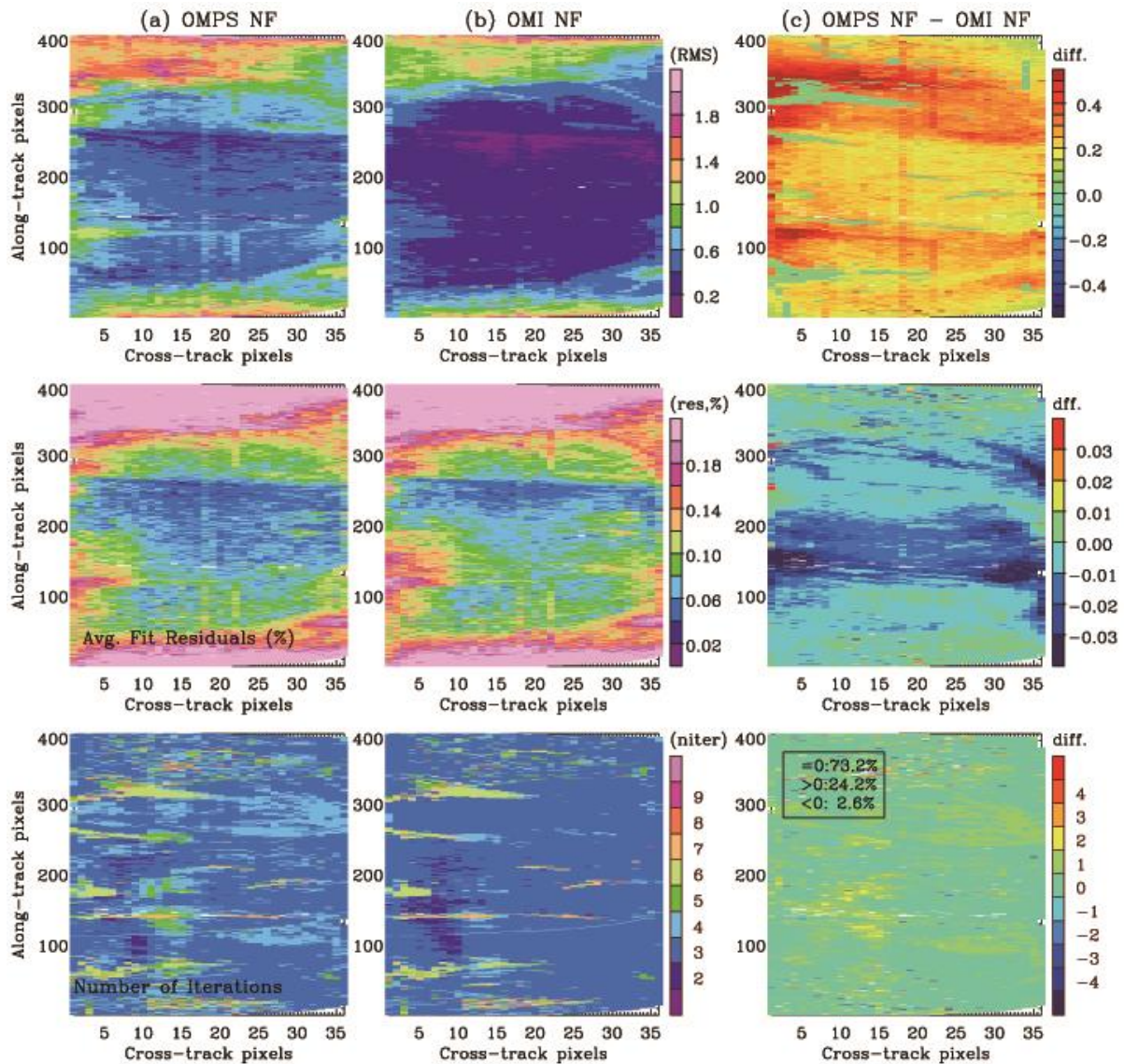
727 Note that OMI noise floor errors (0.4% at wavelengths < 310 nm, and 0.2% at wavelengths > 310 nm) are  
 728 used to define RMS.



729

730 Figure 12. (a) Standard deviations of spectral fitting residuals for 14 March 2013 under clear-sky conditions  
 731 and for small SZAs < 40° (red dotted line), with the 4<sup>th</sup> order polynomial fitting of them (red solid line)  
 732 called “OMPS noise floor (NF) error”. This NF error represents the minimum measurement constraint  
 733 implemented in OMPS ozone fitting process. OMI floor noise error (black line) and OMPS L1B v2.0  
 734 random-noise error (blue line) (orbit: 7132, cross-track: 18, along-track: 200) are also shown for  
 735 comparison in the same panel. (b) OMPS NF at 302.5 nm and 340 nm as a function of SZAs (solid line),  
 736 with the corresponding OMPS L1B v2.0 measurement error (dotted line).

737



738

739 **Figure 13.** Top: Comparison of RMS of fitting residuals relative to the assumed measurement errors as  
 740 functions of cross-track and along-track pixels for orbit 7132 with (a) OMPS NF (first column) and (b)  
 741 OMI NF (second column), respectively, with (c) their absolute differences (third column). The definition of  
 742 RMS is given in Fig. 11. Middle: Comparison of average fitting residuals relative to the simulated radiances  
 743 (%), which are similar to RMS, except that radiance differences are normalized to measured radiances  
 744 instead of measurement errors. Bottom: Comparison of the number of the retrieval iterations.

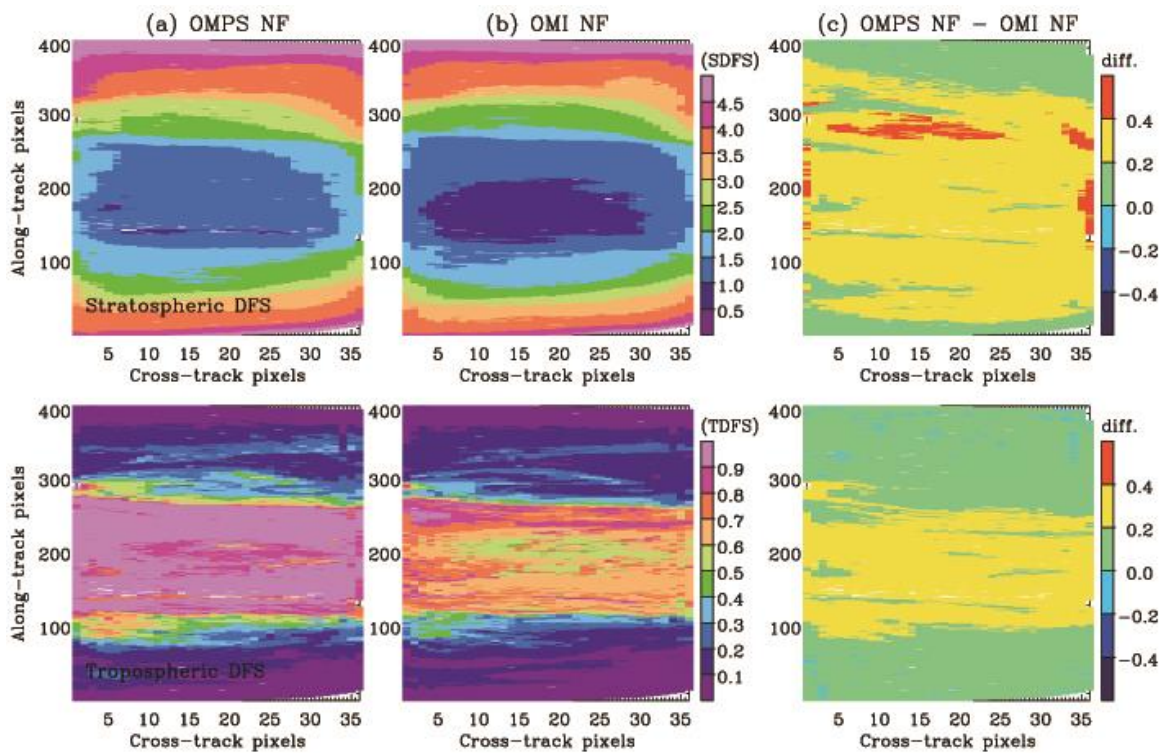
745

746

747



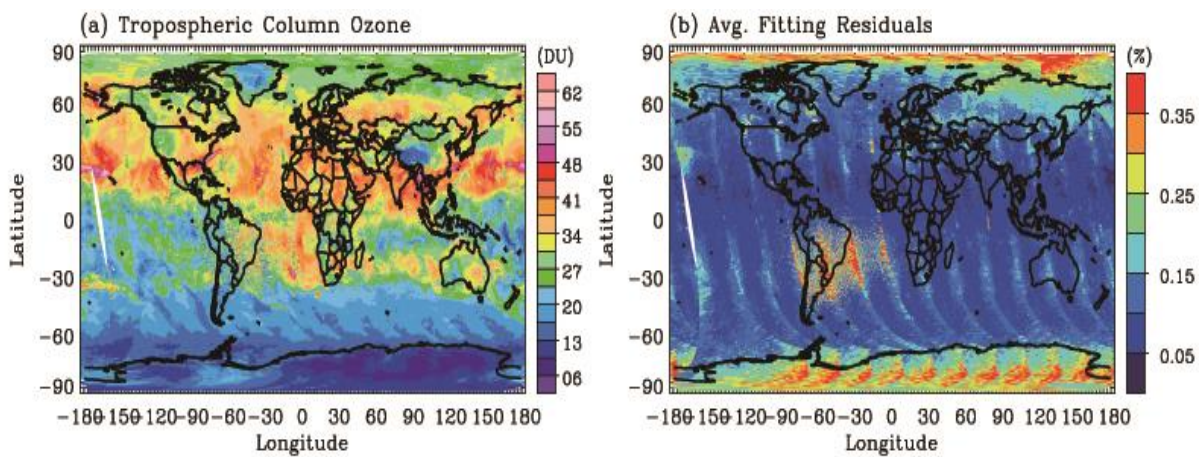
748  
749



750

751 **Figure 14. Same as Fig. 13, but for the integrated Degrees of Freedom for Signal (DFS) in the stratosphere**  
752 **(top) and troposphere (bottom), respectively.**

753



754

755 **Figure 15. (a) Same as Fig 7.b, but for improved retrievals with common mode correction and OMPS noise**  
756 **floor error, (b) corresponding average fitting residuals (%).**